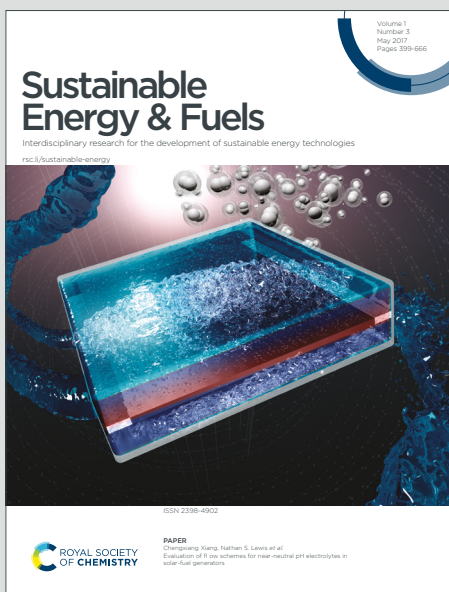


Sustainable Energy & Fuels

Interdisciplinary research for the development of sustainable energy technologies

Accepted Manuscript

This article can be cited before page numbers have been issued, to do this please use: A. Malek, A. Hoang, T. Islam, M. A. Hasnat, T. Islam and A. Islam, *Sustainable Energy Fuels*, 2026, DOI: 10.1039/D5SE01485A.



This is an Accepted Manuscript, which has been through the Royal Society of Chemistry peer review process and has been accepted for publication.

Accepted Manuscripts are published online shortly after acceptance, before technical editing, formatting and proof reading. Using this free service, authors can make their results available to the community, in citable form, before we publish the edited article. We will replace this Accepted Manuscript with the edited and formatted Advance Article as soon as it is available.

You can find more information about Accepted Manuscripts in the [Information for Authors](#).

Please note that technical editing may introduce minor changes to the text and/or graphics, which may alter content. The journal's standard [Terms & Conditions](#) and the [Ethical guidelines](#) still apply. In no event shall the Royal Society of Chemistry be held responsible for any errors or omissions in this Accepted Manuscript or any consequences arising from the use of any information it contains.

1 Synergistic Plasmonic-Semiconductor Heterointerfaces Enabling Efficient 2 CO₂ Hydrogenation to Methanol under Visible-Light Irradiation

4 **Abdul Malek^{a,c}, Anh-Tuan Hoang^d, Md. Tarekul Islam^e, Mohammad A. Hasnat^f, Tarikul
5 Islam^g** Aminul Islam^{a,b,c*}**

6 ^a*Department of Petroleum and Mining Engineering, Jashore University of Science and Technology,
7 Jashore 7408, Bangladesh.*

9 ^b*College of Engineering, Korea University, 145 Anam-ro, Seongbuk-gu, Seoul 02841,
10 Republic of Korea.*

11 ^c*Hydrogen Energy and CO₂ Conversion Lab, Department of Petroleum and Mining Engineering,
12 Jashore University of Science and Technology, Jashore 7408, Bangladesh.*

13 ^d*Dong Nai Technology University, Vietnam*

14 ^e*Department of Leather Engineering, Faculty of Mechanical Engineering, Khulna University of
15 Engineering and Technology, Khulna 9203, Bangladesh.*

16 ^f*Department of Chemistry, School of Physical Sciences, Shahjalal University of Science and
17 Technology, Sylhet 3114, Bangladesh.*

18 ^g*Department of Textiles, Merchandising, and Interiors, University of Georgia, Athens, Georgia
19 30602, United States.*

21 *Corresponding authors: aminul_pme@just.edu.bd (A. Islam); tarikul@uga.edu (T. Islam)

23 Abstract

24 The photocatalytic conversion of carbon-dioxide (CO₂) to methanol (CH₃OH) under mild
25 conditions has been regarded as a promising, cost-effective, and environmentally sustainable
26 approach for carbon utilization and renewable fuel generation. However, the process has been
27 hindered by limited charge separation efficiency and insufficient CO₂ activation. In this study,
28 a heterostructured Ag–Si/MgO/ZnO photocatalyst was rationally designed and synthesized via
29 a solid-phase reaction method. A CH₃OH production rate of 357.53 μmol g_{cat}⁻¹ h⁻¹ was
30 achieved over the optimized 10% Ag–Si/MgO/ZnO composite catalyst at 250 °C, representing
31 a substantial enhancement compared to the Si/ZnO and Si/MgO/ZnO photocatalysts. The
32 CH₃OH production performance was found to be higher in the photocatalyst/gas-phase system
33 than that reported in comparable studies. The theoretical activation energy for Ag–
34 Si/MgO/ZnO was found to be 158.14 kJ mol⁻¹, which is lower than that of Si/MgO/ZnO
35 (167.79 kJ mol⁻¹) and Si/ZnO (177.97 kJ mol⁻¹), indicating enhanced CO₂ activation and



36 higher CO₂ conversion. More importantly, after more than 72 h of irradiation, the system still
37 exhibited a high CH₃OH production rate, demonstrating its potential for practical application.

View Article Online
DOI: 10.1039/DSE01485A

39 **Keywords:** Photocatalyst, hydrogenation, synergistic effect, carbon-dioxide photoreduction.

40

41 1. Introduction

42 The average concentration of CO₂ has jumped to 427.48 ppm in the atmosphere currently.¹
43 Although the concentration level of CO₂ in the atmosphere shouldn't be higher than 350 ppm.
44 The sharp rise of concentration of CO₂ into the atmosphere is the main driver of greenhouse
45 effect which causes global warming and climate change, gravely affecting human beings ability
46 to live normally. Therefore, limiting the release of CO₂ is a significant task for humankind in
47 an attempt to mitigate global warming. The production of liquid fuels and value-added
48 chemicals via CO₂ hydrogenation has recently gained significant attention due to its promising
49 economic potential and environmental advantages.²⁻⁴ Various value-added chemicals including
50 CH₃OH, CH₄, CH₃CH₂OH, olefins, DME etc. are obtained from hydrogenation of CO₂.^{5,6}
51 Among different products, CH₃OH has extensive applications as a vital organic solvent. It is
52 an essential organic feedstock for organic synthesis, including the production of HCHO,
53 C₃H₆O₃, C₂H₄, CH₃COOH, and other substances. It is also utilized as a hydrogen transporter,
54 and as an energy source for fuel cells and gasoline.^{7,8} Consequently, the process of
55 hydrogenation of CO₂ into CH₃OH utilizing green H₂ has garnered a lot of interest recently.^{9,10}

56 CO₂ hydrogenation to CH₃OH had been extensively studied. For instance, new active
57 sites were introduced through nitrogen doping by Yang et al.,¹¹ which resulted in significant
58 enhancement of reaction activity and catalytic stability of In₂O₃. Using an In₂O₃ nano-catalyst,
59 a CH₃OH selectivity of 62.3% was achieved at 300 °C and 5 MPa. The ZrO₂/Cu photocatalyst
60 was reported to have exhibited strong activity for CH₃OH formation. The hydrogenation of
61 surface oxygenate intermediates and the activation of CO₂ were found to have been
62 significantly enhanced over these configurations. In Cu-based catalysts, the promotion of
63 CH₃OH synthesis was observed when Zn species were incorporated. The presence of Zn
64 species was found to have increased the dispersion of Cu particles and prevented their
65 agglomeration. As a result, a high copper surface area was maintained on the catalyst, which
66 was considered to have improved its performance in CH₃OH synthesis. Moreover, the
67 incorporation of ZnO was observed to have strengthened the resistance of Cu particles to



68 poisoning, improved CO₂ adsorption on the catalyst surface, and provided a higher density of
69 catalytically active sites for the reactants.

70 Single-component photocatalysts had typically been limited by poor visible-light
71 utilization, fast electron–hole recombination, and unfavorable adsorption energetics for key
72 CO₂-reduction intermediates, whereas complementary metals had been shown to adjust charge-
73 transfer pathways and intermediate binding in a controllable manner.¹² In bimetallic systems,
74 plasmonic nanoparticles had been expected to generate localized surface plasmon resonance
75 under visible light. As a result, hot-carrier generation and near-field enhancement had been
76 exploited to strengthen light excitation and accelerate electron injection into nearby
77 semiconductor or oxide domains, as widely reported for plasmon-assisted CO₂
78 photoreduction.¹³ Meanwhile, semiconductor domains had been introduced to tune the
79 interfacial electronic structure and adsorption behavior. This approach had allowed early
80 oxygenated intermediates to be stabilized on oxide sites, while hydrogenation-favored steps
81 had been promoted on plasmonic metal sites, in agreement with the principle that bimetallic
82 interfaces enabled spatial separation of adsorption/activation and hydrogenation functions.¹⁴
83 This mechanism had been expected to enhance both activity and selectivity by increasing the
84 supply of reactive electrons from plasmonic components and by optimizing intermediate
85 binding while suppressing unproductive pathways through interfacial site differentiation.¹⁵

86 Elemental Si, a visible-light-responsive semiconductor with a narrow indirect bandgap
87 of ~1.1 eV, enables broad solar absorption and efficient generation of charge carriers under
88 light irradiation, making it highly suitable for solar-driven catalytic applications.¹⁶ When
89 coupled with plasmonic components, Si primarily functions as an electron reservoir and
90 transport medium, facilitating the directional migration of photogenerated or plasmon-induced
91 hot electrons toward catalytically active surface sites. This process promotes interfacial charge
92 separation and effectively suppresses electron–hole recombination through plasmonic–
93 semiconductor coupling and Schottky junction formation.¹⁷ Similar Si-based photocatalytic
94 architectures have been reported to enhance visible-light utilization, charge separation
95 efficiency, and CO₂ reduction performance through plasmonic–semiconductor coupling
96 effects.^{18,19} Plasmonic–semiconductor photocatalysts can utilize up to ~45% of the solar
97 spectrum, significantly improving photon-to-chemical conversion efficiency and reducing
98 external heating energy input.²⁰ By coupling localized surface plasmon resonance (LSPR)–
99 induced hot-electron generation with semiconductor charge transport, the system drives CO₂
100 reduction under mild conditions, thus lowering operational energy requirements per unit



methanol produced. From a techno-economic perspective, visible-light-assisted pathways may become cost-competitive as renewable H₂ prices continue to decline and scalable synthesis routes for plasmonic materials (e.g., Ag, Cu) are further optimized.²¹ Recent analyses suggest that photocatalytic methanol production can be economically favorable when solar-to-fuel efficiencies exceed 5–8% and catalyst stability surpasses several thousand hours.²² Although further development is needed, the combination of low-temperature operation, reduced energy intensity, and the prospect of using abundant, sunlight-driven excitation underscores the long-term economic viability of plasmonic–semiconductor photocatalysts for sustainable CO₂ valorization.

Visible-light-driven CH₃OH synthesis over plasmonic Cu/ZnO catalysts, achieving a CH₃OH production rate of 127.8 μmol g⁻¹ h⁻¹, was reported by Wang and co-workers.²³ It was found that, despite these advancements, copper-based catalysts were still prone to favor the reverse water–gas shift (RWGS) reaction. This undesired pathway was identified as a major limitation to the selective hydrogenation of CO₂ into CH₃OH and other value-added products when thermal heterogeneous catalysts were employed. To mitigate sintering and enhance catalyst stability, various promoters such as Al₂O₃, MgO, SiO₂, CeO₂, and ZrO₂ were commonly incorporated.²⁴ Among these, MgO was recognized as a promising promoter owing to its unique physicochemical properties. MgO was reported to inhibit the RWGS reaction and function as an adsorbent carrier with desirable features such as large surface area, high density of adsorption sites, tunable surface properties, and high chemical reactivity. Mg-based catalysts were reported to exhibit excellent performance for CO₂ hydrogenation to hydrocarbons. The incorporation of MgO as a catalyst component led to enhanced CO₂ adsorption due to its basic nature and improved metal dispersion by increasing surface area as a result of its low density. Few studies had been conducted on MgO-based catalysts for CO₂ hydrogenation to CH₃OH, and MgO was generally combined with other catalytic components to improve overall performance. For example, the influence of Cu/MgO/Al₂O₃ catalysts was investigated by Dasireddy et al.,²⁵ and the Cu/MgO/Al₂O₃ sample was reported to display the highest activity, which was attributed to the increased number of active sites for CO₂ and H₂ adsorption provided by MgO. Using a Cu–ZnO/MgO catalyst, Guo et al. achieved a CO₂ conversion of 7.6% and a CH₃OH selectivity of 91% at 200 °C and 5 MPa.²⁶ These findings demonstrated that high CH₃OH selectivity could be achieved through conventional heterogeneous catalysis. Nevertheless, because of the inherent thermodynamic stability of CO₂, its hydrogenation to CH₃OH was typically carried out under relatively harsh conditions, requiring elevated temperatures (>200 °C) and high pressures (>4 MPa).



135 Doping was adopted as a standard modification strategy and was increasingly focused
136 upon by researchers. Among the various modification approaches applied to ZnO or MgO
137 carriers, the incorporation of metals was predominantly employed. Noble metals were
138 considered effective cocatalysts for charge carrier separation, as they were believed to act as
139 electron sinks and solid-state mediators. Catalysts based on noble metals such as Pd, Pt, and
140 Au were reported to exhibit excellent hydrogen spillover capacity, high stability, and strong
141 anti-sintering ability in the CO₂-to-CH₃OH reaction.²⁷ For instance, oxygen vacancies were
142 introduced on the surface of Pd/In₂O₃ catalysts by Men et al.,²⁸ resulting in a CH₃OH yield of
143 8.9% with a CO₂ conversion of 24.5%. Similarly, a 2 wt.% Pd/CeO₂ catalyst was reported by
144 Pothu et al. to have achieved a CO₂ conversion of 49.6% and a CH₃OH selectivity of 69.5%.²⁹
145 In another study, CO₂ hydrogenation with H₂ over a Pt/film/In₂O₃ catalyst was reported by
146 Men and co-workers, achieving a CO₂ conversion of 37.0% and a CH₃OH selectivity of 62.6%.
147 Sun et al. confirmed,³⁰ both theoretically and experimentally, the feasibility of selective CO₂
148 hydrogenation to CH₃OH over Ag/In₂O₃. Under reaction conditions of 300 °C and 5 MPa,
149 CH₃OH selectivity of 58.2% was maintained with a CO₂ conversion of 13.6% and a space-
150 time yield (STY) of 0.453 g_e g_a g⁻¹h⁻¹. The appropriate selection of dopant metal into
151 the metal oxide catalyst was reported to enhance interfacial charge transfer, thereby
152 significantly improving CO₂ adsorption. Although plasmonic–semiconductor hybrid systems
153 have been investigated under photothermal conditions, where thermal effects predominantly
154 govern the catalytic activity,^{31–34} studies focusing on photocatalytic CO₂ conversion driven by
155 plasmon-induced charge separation particularly in silicon-based, cost-effective semiconductor
156 platforms remain limited.

157 In this study, a plasmonic Ag–Si/MgO/ZnO composite photocatalyst was synthesized
158 via a solid-phase reaction method, and its photocatalytic performance was evaluated for CO₂
159 conversion under visible-light irradiation. Bimetallic Ag and Si species were introduced as
160 cocatalysts supported on an MgO promoter to enhance charge separation efficiency and overall
161 catalytic activity of the Ag–Si/MgO/ZnO system. The photocatalytic performance was
162 systematically investigated in terms of product yield and apparent quantum yield (AQY).
163 Furthermore, surface activation, structural evolution, and catalyst stability under extended
164 illumination were analyzed using a suite of advanced characterization techniques. The findings
165 reveal that the engineered heterostructure exhibits excellent stability, high photocatalytic
166 efficiency, and strong scalability potential, offering valuable insights into the rational design
167 of next-generation plasmonic–semiconductor systems for solar-driven CO₂ reduction.

168 **2. Materials and Methods**169 **2.1 Materials**

170 Mg powder (99%), Zn powder (99%), and Silver Nitrate (AgNO_3), tri-Sodium citrate dehydrate
171 ($\text{C}_6\text{H}_5\text{Na}_3\text{O}_7\cdot2\text{H}_2\text{O}$), Sodium Borohydride (NaBH_4) were purchased from Sigma-Aldrich
172 (USA). Ultra-pure water was supplied through distillation of water. CO_2 (99.99%) and N_2
173 (99.99%) were collected from Spectra International Limited, Bangladesh. Water is electrolyzed
174 to deliver renewable H_2 (99.99%). The electrolyte, Na_2SO_4 (99.99%) utilized to electrolyze
175 water, was purchased from Sigma-Aldrich (USA). All chemicals used in this work were
176 employed without any additional treatment.

177 **2.2 Synthesis of SiO_2**

178 Through the calcination procedure, waste rice husk was converted into a precursor silica (SiO_2)
179 nanopowder. The wasted rice husk was first acid purified by immersing it in a 1000 ml aqueous
180 solution of 20% HCl in a beaker and heating it to 100 °C for six hours. After being cleaned
181 three times with pure water, the deep yellow rice husk was taken out from the beaker. The
182 cleaned rice husk was then dried in an oven for 12 hours at 90 °C. To calcine the sample, the
183 dried rice husk was placed in a tube furnace with the aid of a ceramic crucible and heated to
184 800 °C for two hours at a ramping rate of 10 °C min⁻¹. The bright white SiO_2 powder was
185 collected when it had attained room temperature.

186 **2.3 Synthesis of Si/MgO/ZnO**

187 To develop a semiconductor-based photocatalyst, solid combustion approach was utilized in a
188 specifically developed sealed stainless steel reactor. Employing a single-step magneto-thermic
189 reduction technique, a Si/MgO/ZnO composite was developed in an enclosed reactor. Initially,
190 1 g of the obtained SiO_2 nanopowder was finely grounded with 0.65g of Zn powder and 0.65g
191 of Mg powder by following the proportions of SiO_2 , Zn, and Mg being 1: 0.65: 0.65. Then, the
192 sealed stainless steel reactor was filled with the grounded mixture of SiO_2 , Zn, and Mg
193 powders. To execute the magneto-thermic conversion, the enclosed stainless steel reactor was
194 placed within a muffle furnace and heated to 800 °C for 6 h, raising the temperature by 5 °C per
195 minute. The reactor was removed from the furnace once it reached room temperature.
196 The built Si/MgO/ZnO material was removed from the reactor and finely powdered.

197

198 **2.4 Synthesis of Ag nanoparticles (NPs)**View Article Online
DOI: 10.1039/D5SE01485A

199 Ag nanoparticles (Ag NPs) were synthesized via a chemical reduction method employing tri-
200 sodium citrate ($C_6H_5Na_3O_7 \cdot 2H_2O$) and sodium borohydride ($NaBH_4$) as reducing agents.
201 Silver nitrate ($AgNO_3$) and $Na_3C_6H_5O_7$ were used as precursors, and all solutions were freshly
202 prepared using distilled water. In a typical procedure, 100 mL of 1 M $Na_3C_6H_5O_7$ solution was
203 magnetically stirred, after which 100 mL of 0.25 mM $AgNO_3$ solution was added dropwise
204 under continuous stirring until a clear and homogeneous solution was obtained. Subsequently,
205 250 mL of 148 mM $NaBH_4$ solution was introduced dropwise at a controlled rate of
206 approximately one drop per second. The reaction mixture was stirred vigorously for 6 h, during
207 which a gradual color transition from light yellow to dark yellow and finally to gray was
208 observed, indicating nanoparticle formation and subsequent colloid destabilization. After
209 completion of the reaction, stirring was stopped, and the solution was left undisturbed overnight
210 to allow complete precipitation of the nanoparticles. The resulting Ag nanoparticles had been
211 collected as a solid residue, repeatedly washed with distilled water to remove impurities, and
212 subsequently subjected to high-temperature treatment (850 °C for 6 h) during photocatalyst
213 preparation. Therefore, any residual species would have been expected to be removed through
214 post calcination process.

215 **2.5 Synthesis of Ag-Si/MgO/ZnO**

216 With the aid of a hydraulic pressure machine, the fine Ag-Si/MgO/ZnO mixture powder were
217 further sealed in a cylindrical stainless steel reactor under elevated pressures. Attempting to
218 build a solid Ag-Si/MgO/ZnO structure, the reactor was then placed inside a muffle furnace
219 and heated to 850 °C for 6 h, raising in temperature by 5 °C per minute. When the reactor
220 reached room temperature, it was removed from the furnace. Employing a hydraulic pressure
221 machine, the Ag-Si/MgO/ZnO specimen with a solid structure was removed from the reactor.
222 After being cleaned the surface of the formed solid Ag-Si/MgO/ZnO specimen with series
223 paper, it was heated in a Muffle furnace for two hours at a temperature of 5 °C per minute. The
224 solid-structured Ag-Si/MgO/ZnO composite was subsequently removed from the furnace and
225 split it into several pieces to be used as a photocatalyst in a continuous flow reactor once it had
226 reached room temperature. For the purpose to assess the photocatalytic efficiency, additional
227 Si/MgO/ZnO and Si/ZnO catalysts were developed without Ag or Ag/MgO, respectively. The
228 overall synthesis process of Ag-Si/MgO/ZnO photocatalyst is presented in Fig. S1.

229 **2.2 Characterization**View Article Online
DOI: 10.1039/D5SE01485A

230 The microstructure and morphology of the prepared materials were characterized by scanning
231 electron microscopy (SEM, Sigma-300, Germany), while elemental composition and mapping
232 were determined by energy-dispersive spectroscopy (EDS). Transmission electron microscopy
233 (TEM) and high-resolution TEM (HRTEM) images with elemental mapping were obtained
234 using FEI Talos F200X and Tecnai F20 instruments. The crystalline phases were analyzed by
235 X-ray diffraction (XRD, Bruker AXS, Germany) using Cu K α radiation ($\lambda = 1.5418 \text{ \AA}$). Optical
236 absorbance and diffuse reflectance spectra were recorded using a Cary 5000 UV-vis
237 spectrophotometer (Varian, USA) and a Thermo Scientific Evolution 220 UV-vis DRS
238 instrument, respectively. Surface composition and chemical states were examined by X-ray
239 photoelectron spectroscopy (XPS, ESCALAB 250Xi, Thermo Fisher, UK), and
240 photoluminescence (PL) spectra of the solid powders were measured with a Hitachi F-7000
241 fluorescence spectrophotometer (Japan).

242 **2.4 Photo-electrochemical tests**

243 The CorrTest electrochemical workstation (Wuhan Corrtest Instruments Comp. Ltd., China)
244 was utilized to measure the transient photocurrent response of all samples. The electrochemical
245 impedance spectroscopy, and Mott-Schottky plots of catalyst specimens were performed on
246 the Autolab workstation (Netherlands). A platinum wire served as the counter electrode. An
247 Ag/AgCl electrode was used as the reference electrode. A conventional quartz cell with three-
248 electrode was employed in both the electrochemical system. The solution of 0.5 M Na₂SO₄ was
249 used as electrolyte. The series of photocatalyst films were coated on fluorine-tin-oxide (FTO)
250 glasses of 1 cm² area using as a working electrode. The working electrodes were prepared using
251 doctor blade method. In short, before preparing the solution, the polyvinylidene difluoride
252 (PVDF) binder was dried over an entire night. N-methyl-2-pyrolidone (NMP) solvent was
253 utilized to combine 90% active material (photocatalyst) and 10% binder agent (PVDF) to
254 prepare a paste. Employing a doctor blade approach, the as-prepared paste was placed on the
255 functionalized surface of the FTO glass. The decorated FTO was placed in an oven for 24 hours
256 at 60 °C for drying it properly. A tungsten lamp (100W) was utilized to illuminate the prepared
257 samples. N₂ gas was used to purge the electrolyte for 30 minutes prior to the tests. In a 0.5 M
258 Na₂SO₄ solution, electrochemical impedance spectroscopy (EIS) was conducted at a frequency
259 ranging from 0.1 Hz to 1000 Hz. In each instance, a sinusoidal potential amplitude of 5 mV was
260 applied. Mott-Schottky plots was performed utilizing the same setup (applied voltage: -0.5 V,



frequency: 1000 Hz, AC voltage: 5 mV amplitude). Over the course of on-off cycle, the transient photocurrent responses were measured at 0 V potential bias versus Ag/AgCl.

2.5 Photocatalytic performance test

The schematic diagram of experimental set up for photocatalytic CO₂ hydrogenation to CH₃OH under visible light is presented in Fig. S2. Utilizing the prepared catalyst, a cylindrical fixed-bed continuous-flow quartz-glass reactor was employed to measure the hydrogenation of CO₂ to CH₃OH. The reactor is made up of a 130 mm length and 8 mm diameter column. 1 g of photocatalyst (40–50 mesh) was installed in the middle part of column almost 10 mm in length. By filling both sides of the photocatalyst bed with quartz wool, the catalyst bed maintained fixed. The reactor was installed in a cylindrical glass furnace 4 cm away from the light source and linked to the gas inlet and outlet. An electric heater is fitted into the furnace to control the temperature of the reactor. A thermocouple is fitted in the furnace to measure the inside temperature of the furnace. A mass flow controller was employed to control the flow rate of the reactant gas mixture. For maintaining a specified pressure, a back-pressure controller was integrated into the gas line which was connected to the outlet. The reaction was carried out at atmospheric pressure during reaction circumstances with a N₂ flow along with temperature ranges up to 300 °C. Following 3 h, H₂ (generated by electrolysis) and CO₂ (99.999%) were provided throughout the reaction. In all experiments using the reaction mixture, we used the ratio H₂:CO₂=3:1 that reflects a stoichiometric equation for the CH₃OH synthesis reaction (CO₂ + 3H₂ → CH₃OH + H₂O) and has been commonly used in related prior studies. The kinetic study on the reaction was carried out between 200 °C and 300 °C. The liquid phase products (CH₃OH) resulting from photocatalytic CO₂ reduction were collected in a cold trap and subsequently analyzed on gas chromatography (GC-2014, SHIMADZU) equipped with flame ionization detector (FID). The production rate of CH₃OH in the hydrogenation of CO₂ was determined by the following Eq. (3):³⁵

$$\text{CH}_3\text{OH yield rate} = \frac{\text{amount of produced CH}_3\text{OH}}{\text{mass of photocatalyst} \times \text{time duration}} \text{ } \mu\text{mol g}^{-1} \text{ h}^{-1} \quad (3)$$

The apparent quantum yield of the as-prepared Ag-Si/MgO/ZnO photocatalyst for CH₃OH production was evaluated by using the following Eq. (4).³⁵

Apparent quantum yield for CH₃OH,

$$\text{AQY} = \frac{6 \times \text{Number of CH}_3\text{OH molecules}}{\text{Number of incident photons}} \times 100\%$$

$$291 \quad = \frac{6 \times N_{CH_3OH} \times N_A}{I_i \times A \times \frac{\lambda}{hc} \times t} \times 100\%$$

View Article Online
DOI: (4) 10.1039/D5SE01485A

292 Where N_{CH_3OH} was defined as the number of moles of CH_3OH that were generated during the
293 time interval t . The Avogadro's number was taken as $(6.023 \times 10^{23} \text{ atoms.mol}^{-1})$. The area
294 of the surface on which the light was irradiated was denoted as A (m^2). Planck's constant, h
295 was considered as $(6.626 \times 10^{-34} \text{ Js})$; and the speed of light, c was taken as $3 \times 10^8 \text{ ms}^{-1}$,
296 The time duration of light irradiation was represented as t (s). The wavelength of the incident
297 light, λ was measured by a bandpass filter and was taken as $\lambda=420 \text{ nm}$. The average intensity
298 of the incident light, I_i , was measured by a suitable measuring instrument, such as a
299 pyranometer, and was expressed in $W\text{m}^{-2}$.

300

301 **2.6 Computational Methods**

302 The distribution of electro-magnetic (EM) field over the Si/ZnO, Si/MgO, Si/ZnO/MgO, and
303 Ag-Si/ZnO/MgO are conducted using finite-difference time-domain (FDTD) method. The 630
304 nm is used as the simulated excitation wavelength of all nano-structures. The Ag-Si/ZnO/MgO
305 is modeled as follows: isolated Si, Si/MgO and Ag-Si/MgO NPs assemblies are placed on the
306 surface of ZnO nanosheets, respectively. A plane wave propagating in the z-direction with an
307 electric field parallel to the x-direction was selected to estimate the electric field distribution.
308 The dielectric functions of Ag, Si, MgO, and ZnO were taken from the literature. Density
309 functional theory (DFT) calculations were carried out using the DMol³ module within the
310 Materials Studio software package. The interaction between ionic cores and valence electrons
311 was modeled using the projector augmented-wave (PAW) formalism. The plane-wave basis
312 set was constructed with a kinetic energy cutoff of 500 eV to ensure adequate convergence.
313 Exchange–correlation effects were accounted for within the framework of the generalized
314 gradient approximation (GGA), employing the Perdew–Burke–Ernzerhof (PBE) functional.
315 Brillouin zone integrations were performed using Monkhorst–Pack k-point meshes. For the
316 slab models considered, a final k-point mesh of $X \times Y \times 1$ was adopted, where X and Y were
317 determined from the convergence tests. A single k-point was used along the surface normal
318 due to the large vacuum spacing. Self-consistent field (SCF) cycles were converged to a
319 tolerance of $1 \times 10^{-5} \text{ eV/atom}$, with convergence thresholds of $0.1 \text{ eV/}\text{\AA}$ for maximum forces
320 and $5 \times 10^{-3} \text{ \AA}$ for atomic displacements.

321

322

323 The Gibbs free energy for all reactions was obtained by the following formula Eq.(5):³⁶ View Article Online
 DOI: 10.1039/D5SE01485A

324 $\Delta G = \Delta E + \Delta ZPE - T\Delta S$ (5)

325 Here, ΔE denotes the total energy change calculated using Materials Studio, while ΔZPE and
 326 ΔS correspond to the variations in zero-point energy and entropy, respectively. The values of
 327 ΔE , ZPE , ΔZPE and $T\Delta S$ are calculated by the following supplementary Eqs. S1-S4. The
 328 change of zero point energy and change of TS for various reactions in the CO_2 hydrogenation
 329 to CH_3OH are calculated by the pathways following in Table 1.

330 **Table 1:** Calculation of change of zero point energy and change of TS for various reactions in
 331 the CO_2 hydrogenation to CH_3OH pathways.

Reactions	Equations for Change of		Value of ΔZPE (eV)	Equations for Change of		Value of $T\Delta S$ (eV)
	ZPE	TS				
$CO_2 + H = COOH$	$\Delta ZPE = ZPE_{COOH} - (ZPE_{CO_2} + ZPE_H)$	$T\Delta S = TS_{COOH} - (TS_{CO_2} + TS_H)$	0.005238155			-1.01506546
$COOH + H = CO + H_2O$	$\Delta ZPE = ZPE_{CO} + ZPE_{H_2O} - (ZPE_{COOH} + ZPE_H)$	$T\Delta S = TS_{CO} + TS_{H_2O} - (TS_{COOH} + TS_H)$	0.010259345			0.83977502
$CO + H = HCO$	$\Delta ZPE = ZPE_{HCO} - (ZPE_{CO} + ZPE_H)$	$T\Delta S = TS_{HCO} - (TS_{CO} + TS_H)$	-0.120043635			-0.27203544
$HCO + H = H_2CO$	$\Delta ZPE = ZPE_{H_2CO} - (ZPE_{CO} + ZPE_H)$	$T\Delta S = TS_{H_2CO} - (TS_{CO} + TS_H)$	-0.114836475			-0.37171585
$H_2CO + H = H_3CO$	$\Delta ZPE = ZPE_{H_3CO} - (ZPE_{H_2CO} + ZPE_H)$	$T\Delta S = TS_{H_3CO} - (TS_{H_2CO} + TS_H)$	-0.132813575			-0.30651881
$H_3CO + H = CH_3OH$	$\Delta ZPE = ZPE_{CH_3OH} - (ZPE_{H_3CO} + ZPE_H)$	$T\Delta S = TS_{CH_3OH} - (TS_{H_3CO} + TS_H)$	-0.084275405			-0.33720159

332

333 The adsorption energy (E_{ads}) was calculated using the following expression:³⁷

334 $E_{ads} = E_{adsorbate+surface} - (E_{adsorbate} + E_{surface})$ (6)

335 Where $E_{adsorbate+surface}$ is the total energy of the surface system after adsorption of the species,
 336 $E_{adsorbate}$ is the total energy of the free adsorbate, and $E_{surface}$ is the total energy of the pristine
 337 surface.

338 3. Result and Discussion

339 The surface activation process for Ag-Si/ZnO/MgO composite photocatalyst is shown in Fig.
 340 1A. Scanning electron microscopy (SEM) analysis was employed to investigate the
 341 morphology of the fabricated Ag-Si/MgO/ZnO catalyst. The Ag-Si/MgO/ZnO catalyst
 342 exhibited densely packed, well-defined cuboidal/prismatic particles with faceted surfaces,
 343 indicative of high crystallinity and uniform growth. These particles exhibit a relatively narrow
 344 size distribution and form an aggregated network with close particle-to-particle contact, as

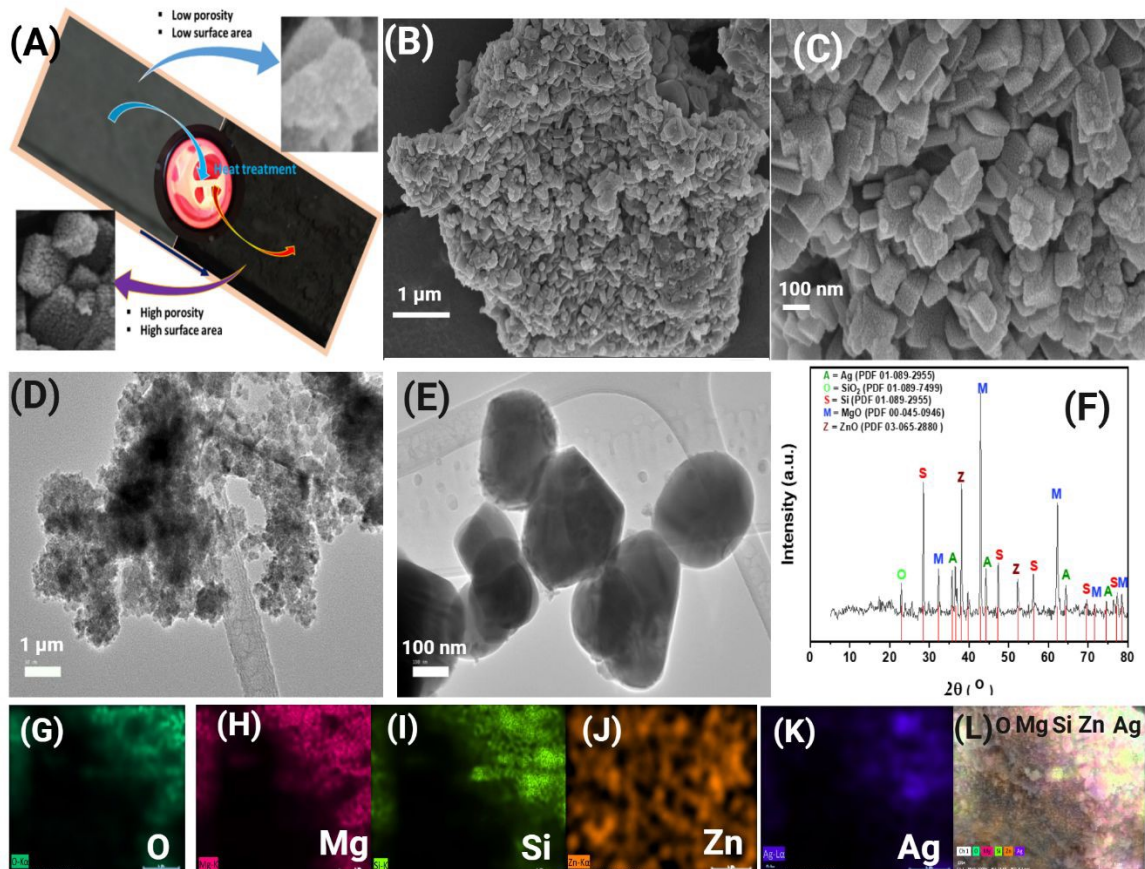
345 depicted in Fig. 1(B-C). The morphology of Ag-Si/MgO/ZnO catalysts was also studied using
346 transmission electron microscopy (TEM). The TEM photograph 1(D-E) displays particles that
347 are well-defined and faceted. Their morphology is polyhedral and appears to be cuboidal or
348 slightly truncated prismatic. The clear edges and uniform contrast show that these are single
349 crystalline domains, not amorphous aggregates. The particle size seen in the TEM is very
350 similar to the size value proposed by the SEM since the size is very monodispersed. Fig. 1(G-L)
351 of the EDX elemental mapping images of the synthesized Ag-Si/MgO/ZnO catalyst showed
352 the distributions of elements Ag, Si, Zn, Mg, and O, thereby confirming successful preparation
353 of the nanocomposite. The elemental mapping of the Ag-Si/MgO/ZnO nanostructured catalyst
354 confirmed the uniform presence of Ag and Si on the nanocrystalline MgO/ZnO support,
355 showing that these elements were evenly spread throughout the catalyst. The Powder XRD
356 analysis showed that all synthesized catalysts are highly crystalline. The XRD pattern of the
357 Ag-Si/MgO/ZnO shows peaks at 28.48°, 42.88°, 56.22°, 69.70°, and 77.38° depicting the
358 indexed peaks (111), (220), (110), (400), and (331) of Si (JCPDS 01-089-2955). The presence
359 of ZnO, MgO and Ag were confirmed by matching the characteristic peaks with their respective
360 JCPDS files (03-65-2880, 00-045-0946, and 01-089-2955).

361

362

View Article Online
DOI: 10.1039/DSE01485A





363
364 Fig. 1 Schematic diagram of the heat-induced surface activation process for Ag-Si/ZnO/MgO
365 composite photocatalyst (A); Morphology of the as-prepared Ag-Si/MgO/ZnO blocks. SEM
366 image of Ag-Si/MgO/ZnO (B-C); TEM images of Ag-Si/MgO/ZnO (D-E); XRD patterns of
367 as-prepared Ag-Si/MgO/ZnO (F); Elemental mapping of Ag-Si/MgO/ZnO EDX analysis (G-
368 L).

369 MgO promotion had been specifically important because MgO had provided basic sites
370 that had strengthened CO₂ adsorption. A higher number of effective adsorption events was
371 maintained compared with supports that were less basic or less able to stabilize highly
372 dispersed metal particles.³⁸ The plasmonic function of Ag had increased the flux of energetic
373 electrons under visible light, while MgO had increased reactant uptake and stabilized interfacial
374 active sites, and this dual promotion had been consistent with the experimentally observed
375 highest methanol rate (357.53 μmol g_{cat}⁻¹ h⁻¹ at 250 °C and 3 bar) and reduced apparent
376 activation energy (158.14 kJ mol⁻¹) for Ag-Si/MgO/ZnO versus the Ag-free counterparts. It
377 was inferred from these results that strong ZnO–MgO interactions occurred which generated



378 high dispersion of Ag and Si species on the surface of the catalyst and small active site
379 formation.

380 All samples were studied under the same condition using the same excitation
381 wavelength of 450 nm in the solid phase to study the charge-carrier dynamics and charge-
382 separation efficiency using photoluminescence (PL) experiments (Fig.2A). Lower PL intensity
383 mean charge separation is more efficient. There was a significantly lower number of
384 recombination events in Ag–Si/MgO/ZnO indicating that the efficiency of charge-separation
385 was excellent for this material. The introduction of Ag into Si/MgO/ZnO likely created
386 additional vacancies that acted as traps for photo-generated charge carriers, thereby
387 significantly suppressing their recombination. This property of keeping electrons in the
388 conduction band for a longer period enhances their photocatalytic activity. The PL quenching
389 effects seen in Ag–Si/MgO/ZnO showed that the charge transfer and separation in the system
390 was enhanced. The outcomes of our PL tests have been confirmed to be consistent with the
391 photocatalytic CO₂ reduction data (Fig 4B–C, E). This means the effective suppression of a
392 result in photo-induced e[−]/h⁺ recombination means the enhancement of observed activity. Ag–
393 Si/MgO/ZnO showed the best performance for CH₃OH production among all tested samples.

394 Enhancing the photocatalytic conversion of CO₂ via Ag–Si/MgO/ZnO heterostructure
395 was due to efficient separation of photo-generated charge carriers. The presence of Ag in Ag–
396 Si/MgO/ZnO made the charge more mobile and limited e[−]/h⁺ recombination. As a result, the
397 transient photocurrent response (Fig.2B) of Ag–Si/MgO/ZnO was about 7.5 times stronger
398 than that of Si/ZnO and 1.8 times stronger than that of Si/MgO/ZnO. The response of the
399 photocurrent remains stable upon repeated on off cycles which indicates a good
400 photoelectrochemical stability that is in line with PL results. Fig.2C presents EIS Nyquist plots
401 (frequency range: 0.1 Hz to 1 kHz, applied bias: −0.5 V. A minor arc radius in the Nyquist plot
402 suggested less resistance to electron migration, signifying efficient charge-carrier separation.
403 The Ag–Si/MgO/ZnO composite had a smaller arc radius than the Si/ZnO and Si/MgO/ZnO
404 with less charge recombination and improved electron–hole migration efficiency. These results
405 were in agreement with the PL spectra. It can be concluded that Ag may play a crucial role in
406 enhancing charge-separation efficiency by suppressing charge-recombination rates and
407 improving the light-absorption behavior. Other researchers also observed that Ag loading
408 effectively suppressed photo-induced electron–hole recombination and increased visible-light
409 absorption, ultimately enhancing photocatalytic activity.³⁹

410

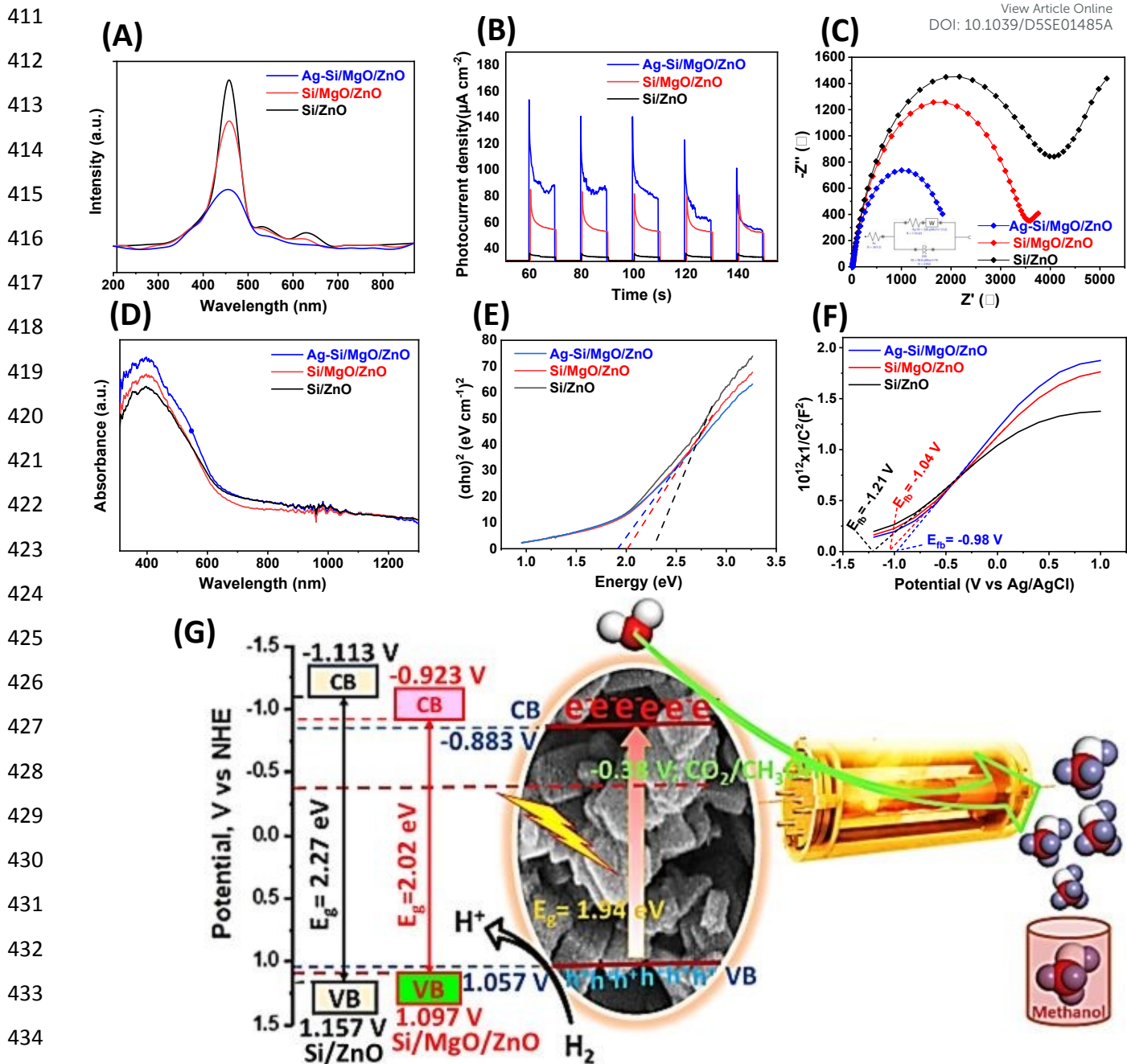


Fig. 2 (A) Photoluminescence (PL) spectra for Si/ZnO, Si/MgO/ZnO, and Ag-Si/MgO/ZnO; (B) Transient photocurrent responses; (C) EIS plots; (D) UV-vis DRS; (E) Tauc's plot of Si/ZnO, Si/MgO/ZnO, and Ag-Si/MgO/ZnO; (F) Mott-Schottky curves; and (G) band alignments of Si/ZnO, Si/MgO/ZnO, and Ag-Si/MgO/ZnO.

The UV-vis diffuse reflectance spectrophotometry studied photocatalysts prepared optical absorption characteristics. The UV-vis diffuse reflectance spectra of Si/MgO/ZnO and Ag-Si/MgO/ZnO are presented in Fig. 2D. The absorption band edge of Si/MgO/ZnO is

444 observed at about 600 nm. After adding Ag nanoparticles, the absorption peak in the visible
 445 range was increased as well as red-shifted to about 630 nm. Thus, the edge of absorption was
 446 changed. The main reason for this change was due to the SPR behavior of the Ag species. Thus,
 447 inclusion of Ag into Ag-Si/MgO/ZnO was found to have greatly enhanced the light-absorption
 448 range into the visible region. Similar observations were made by Chen et al. who realized Ag
 449 doping is responsible for visible light absorption due to plasmon resonance.³⁹ A shift in UV–
 450 vis light absorption toward the visible region after Ag doping was also reported by Chen et al.
 451⁴⁰ However, it was noted that excessive Ag loading resulted in a decline in light absorption and
 452 photocatalytic CO₂ reduction activity, likely due to a shielding effect, where surplus Ag
 453 partially blocked the light absorption of ZnO and MgO. The bandgap (E_g) values of the samples
 454 were estimated using Tauc's relation, as shown in Eq. (6).⁴¹

$$455 \alpha h\nu = A(h\nu - E_g)^n \quad (6)$$

456 Here, A is a constant, E_g represents the semiconductor bandgap, and n is assigned a value of
 457 $\frac{1}{2}$ for a direct bandgap semiconductor. The plots of $(\alpha h\nu)^2$ versus photon energy are generated.
 458 In Fig. 2E, a straight line is fitted to the linear portion of the curve, and this line is extrapolated
 459 to the X-axis to determine the bandgap values. The band-gap values of Si/ZnO, Si/MgO/ZnO
 460 and Ag-Si/MgO/ZnO photocatalysts were derived from Fig. 2E as follows 2.27, 2.02 and 1.94
 461 eV, respectively. The band-gap of Ag-Si/MgO/ZnO is shifted to left after loading of Ag and
 462 improved photocatalytic efficiency for CO₂ reduction. A suitable conduction band edge
 463 position and an adequate supply of free electrons were considered vital for achieving higher
 464 photocatalytic performance. Vu et al. suggested that the conduction band position should have
 465 been more negative than the reduction potential of CO₂ to CH₃OH (−0.38 V, NHE) in order to
 466 enable CH₃OH production.⁴² In this context, Mott–Schottky analysis was carried out to
 467 determine the semiconductor type, and the flat-band potential (E_{fb}) was obtained (Fig. 2F).
 468 Si/ZnO, Si/MgO/ZnO and Ag–Si/MgO/ZnO samples exhibited positive slopes, indicating n-
 469 type semiconductor behavior.⁴³ The flat-band potentials (E_{fb}) of Si/ZnO, Si/MgO/ZnO and Ag–
 470 Si/MgO/ZnO were evaluated to be 1.21 V, −1.02 V and −0.98 V (vs. Ag/AgCl), respectively,
 471 from the Mott–Schottky plots. The E_{fb} values (vs. NHE) for both samples were calculated using
 472 Eq. (7).⁴⁴

$$473 E_{fb} (\text{vs. NHE}) = E_{fb} (\text{vs. Ag/AgCl}) + 0.197 \quad (7)$$

474 The values of E_{fb} (vs. NHE) for Si/ZnO, Si/MgO/ZnO and Ag–Si/MgO/ZnO samples
 475 were determined to be −1.013 V, −0.823 V and −0.783 V, respectively. It was known that the

476 conduction band (CB) position of an n-type semiconductor lies approximately 0.1 eV below
View Article Online
477 E_{fb} .⁴³ Hence, the CB potentials for Si/ZnO, Si/MgO/ZnO and Ag–Si/MgO/ZnO were
DOI: 10.1039/DSE01485A
478 calculated as -1.113 V, -0.923 V and -0.883 V, respectively. The VB positions were then
479 determined to be 1.157 V for Si/ZnO (-1.113 + 2.27), 1.097 V for Si/MgO/ZnO (-0.923 +
480 2.02) and 1.057 V for Ag–Si/MgO/ZnO (-0.883 + 1.94). Ag nanoparticles were found to act
481 as electron-trapping centers, leading to enhanced photocatalytic performance.³⁹ Based on these
482 calculations, experimental data, and CO₂ photoreduction results, a possible band diagram of
483 the as-synthesized photocatalysts was proposed, and the mechanism of CO₂ photoreduction to
484 CH₃OH over the Ag–Si/MgO/ZnO heterostructure was illustrated (Fig. 2G). The conduction
485 band-edge potential of Ag–Si/MgO/ZnO was shown to be more negative than the reduction
486 potential of CO₂ to CH₃OH. Furthermore, the bandgap of Ag–Si/MgO/ZnO was found to be
487 smaller than that of Si/MgO/ZnO. Under visible light illumination, photo-generated electrons
488 were efficiently transferred from the CB of Ag–Si/MgO/ZnO to the Ag NPs. The electrons
489 accumulated on Ag NPs then reduced CO₂ to CH₃OH. The difference in CO₂ photoreduction
490 efficiency between Ag-undoped and Ag-doped Si/MgO/ZnO heterostructures confirmed that
491 the electron transfer rate from Ag NPs to the adsorbed carbonate species was enhanced by Ag
492 integration, which improved carrier separation and overall CO₂ photoreduction efficiency.
493 Additionally, a synergistic effect between ZnO and MgO was postulated to suppress photo-
494 induced charge recombination by transferring photo-generated species from ZnO to MgO
495 within the heterostructure. Thus, the as-prepared Ag–Si/MgO/ZnO heterostructure was found
496 to play a significant role in promoting CH₃OH formation by increasing its production rate. To
497 further elucidate the hydrogenation pathway for CO₂ reduction to CH₃OH over the Ag–Si dual-
498 metal active sites of the Ag–Si/MgO/ZnO catalyst, DFT calculations were carried out using the
499 Material Studio software. The surface electronic state, chemical composition, and bonding
500 environment of the synthesized catalysts were analyzed by X-ray photoelectron spectroscopy
501 (XPS). The XPS spectra of the Ag–Si/MgO/ZnO catalyst were presented in Fig. 3A–E. The
502 full survey spectrum confirmed the presence of Ag, Si, Mg, Zn, and O elements within the
503 sample, which was consistent with the EDS results, thereby indicating the successful synthesis
504 of the catalyst. The characteristic peaks corresponding to Ag 3d, Si 2p, Mg 2p, Zn 2p, and O
505 1s were observed at their respective binding energies.

506 As shown in Fig. 3A, the Ag 3d spectrum exhibited two strong peaks at 367.7 and 374.4 eV,
507 attributed to Ag 3d_{5/2} and Ag 3d_{3/2}, respectively, confirming the presence of metallic Ag
508 clusters. Two weak peaks corresponding to Ag⁺ were also observed, in agreement with the

509 results of Tada et al.,⁴⁵ who reported that XPS spectra displayed peaks for metallic Ag at 368.0
510 eV (Ag 3d_{5/2}) and 374.0 eV (Ag 3d_{3/2}), as well as weak peaks for Ag⁺ at 369.7 eV (Ag 3d_{5/2})
511 and 375.7 eV (Ag 3d_{3/2}).^{46,47} In the Si spectrum (Fig. 3B), peaks at 99.38 and 100.3 eV were
512 assigned to Si 2p_{3/2} and Si 2p_{1/2}, respectively, confirming the coexistence of Ag and Si in the
513 composite. Cerofolini et al. reported that the 2p_{3/2} and 2p_{1/2} peaks in the range of 99–100.5 eV
514 were characteristic of elemental silicon.⁴⁸ The peak at 100.3 eV was assigned to Si–H bonds,
515 while a feature at 532.1 eV indicated the presence of Si–OH species. The presence of Si–H
516 dangling bonds has been associated with enhanced charge separation efficiency on Si-
517 supported photocatalysts.⁴⁹ These functional bonds acted as electron sinks, promoting charge
518 transfer during photocatalysis. In the Mg spectrum (Fig. 3C), two peaks at 49.7 and 50.1 eV
519 were attributed to Mg 2p_{3/2} and Mg 2p_{1/2}, respectively. Fig. 3D shows the Zn 2p spectrum with
520 peaks at 1021.24 eV and 1022.2 eV, corresponding to Zn 2p_{3/2} and Zn 2p_{1/2}, confirming the
521 coexistence of Zn²⁺ and Mg²⁺ species in the catalyst. A higher-binding-energy (~1023.5 eV)
522 in the Zn 2p_{3/2} region could be attributed to surface-defective Zn²⁺ species, originating from
523 oxygen-deficient coordination and/or hydroxylated Zn sites, which result in reduced electronic
524 screening compared to bulk ZnO.⁵⁰ The O 1s spectrum (Fig. 3E) exhibited peaks at 529.7,
525 530.9, and 532.1 eV, assigned to lattice oxygen, oxygen vacancies, and surface hydroxyl
526 groups, respectively. The 529.7 eV peak was consistent with MgO formed through solid-phase
527 oxidation of Mg. The role of MgO as a support was attributed to its tunable acid–base
528 properties, which regulate electron transfer between the support and active phase, as suggested
529 by Julkapli et al.⁵¹ Additionally, Meshkani et al. reported that Lewis basicity of MgO enhanced
530 chemisorption of surface functional groups and promoted electron transport.⁵² No detectable
531 boron-related chemical states had been observed in the XPS spectra, indicating that residual
532 boron-containing species were below the detection limit and negligible in the final material.

533 The total density of states (TDOS) for bimetallic Ag–Si/MgO/ZnO, single-metallic
534 Si/MgO/ZnO, and Si/ZnO catalysts are presented in Fig. S3. The TDOS of bimetallic Ag–
535 Si/MgO/ZnO exhibited a narrower bandgap compared to Si/MgO/ZnO and Si/ZnO, justifying
536 its faster electron excitation and transfer to intermediate species. The bimetallic co-catalyst
537 thus accelerated electron transport, enabling the six-electron reduction of CO₂ to CH₃OH.
538 Projected partial density of states (PDOS) analysis (Fig. 3F) showed that the s-band center of
539 Ag–Si/MgO/ZnO was located near the Fermi level (E_F), favoring activation of O-species
540 adsorption. The weak s–p orbital overlap indicated a long-range interlayer interaction, allowing
541 CO₂ molecules to pass through easily without significantly affecting the catalyst interface.



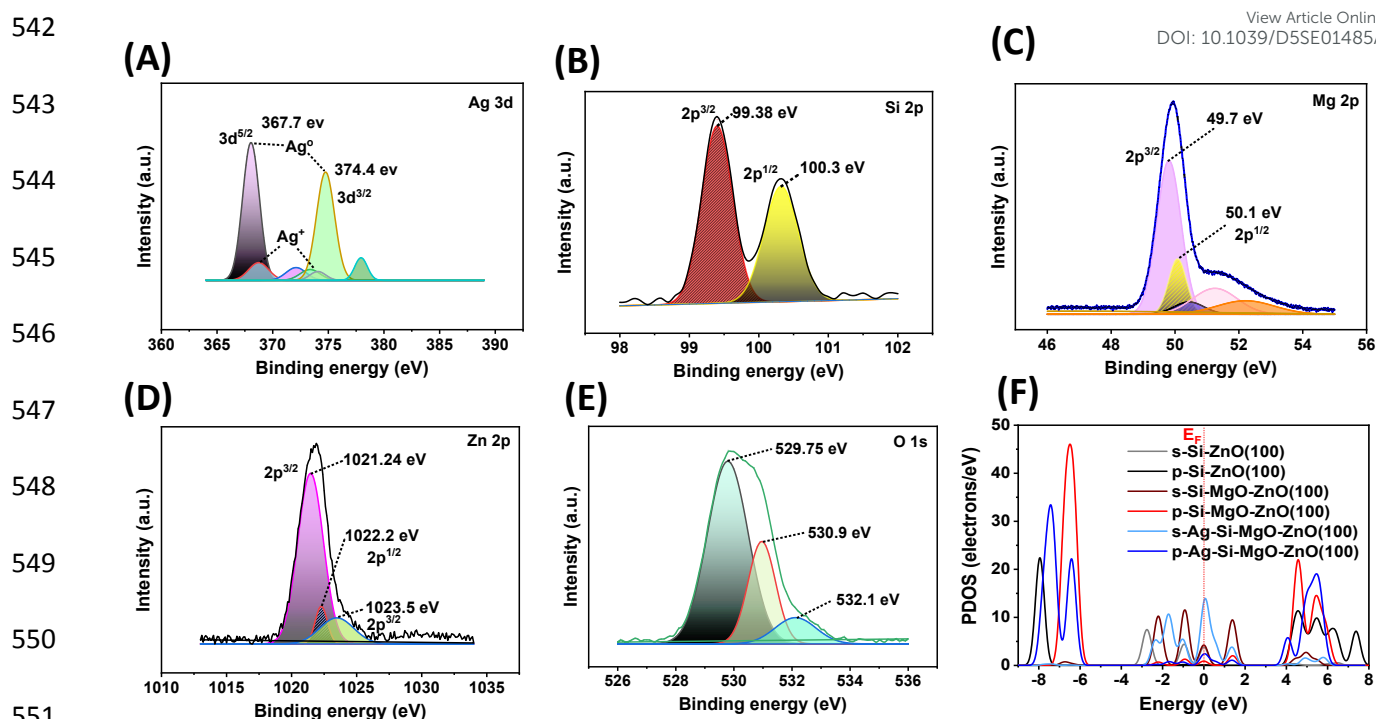
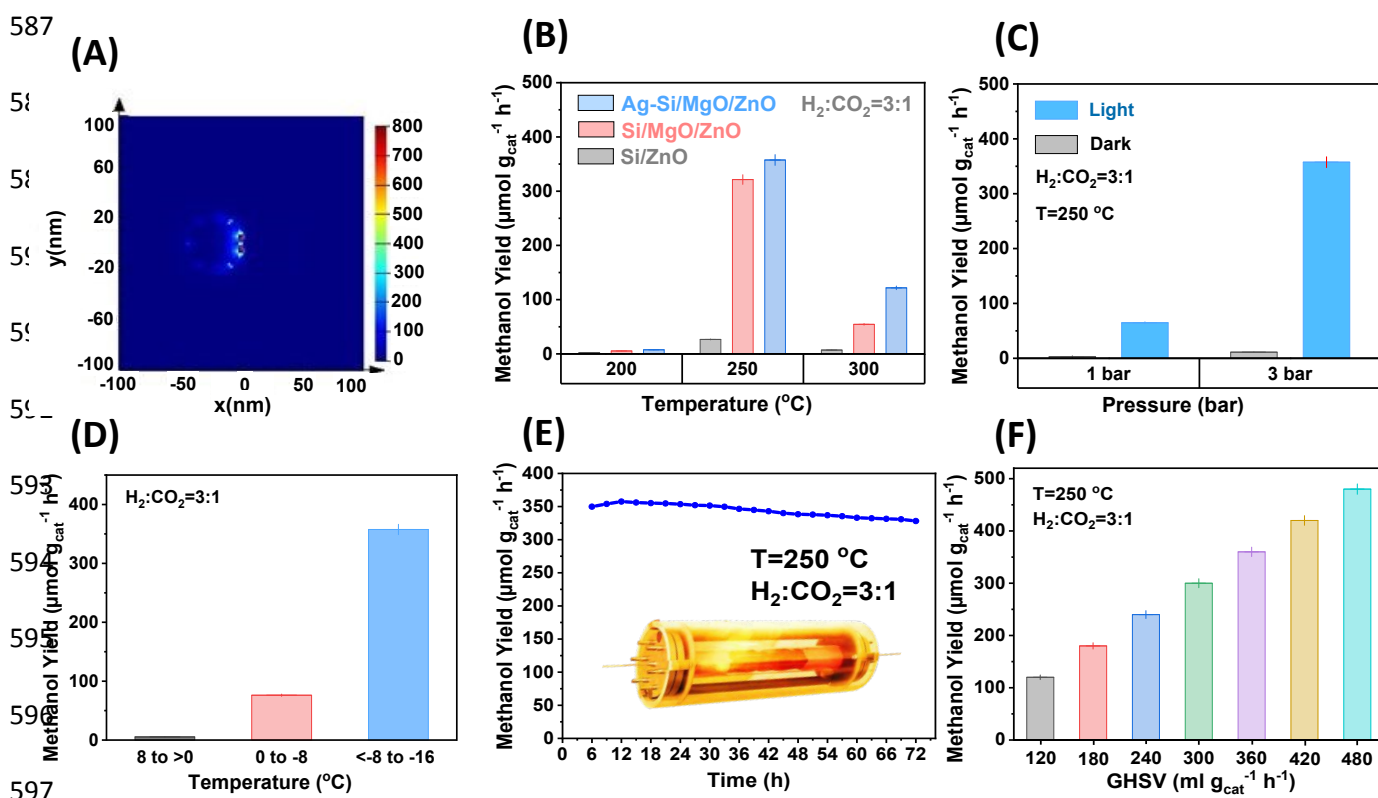


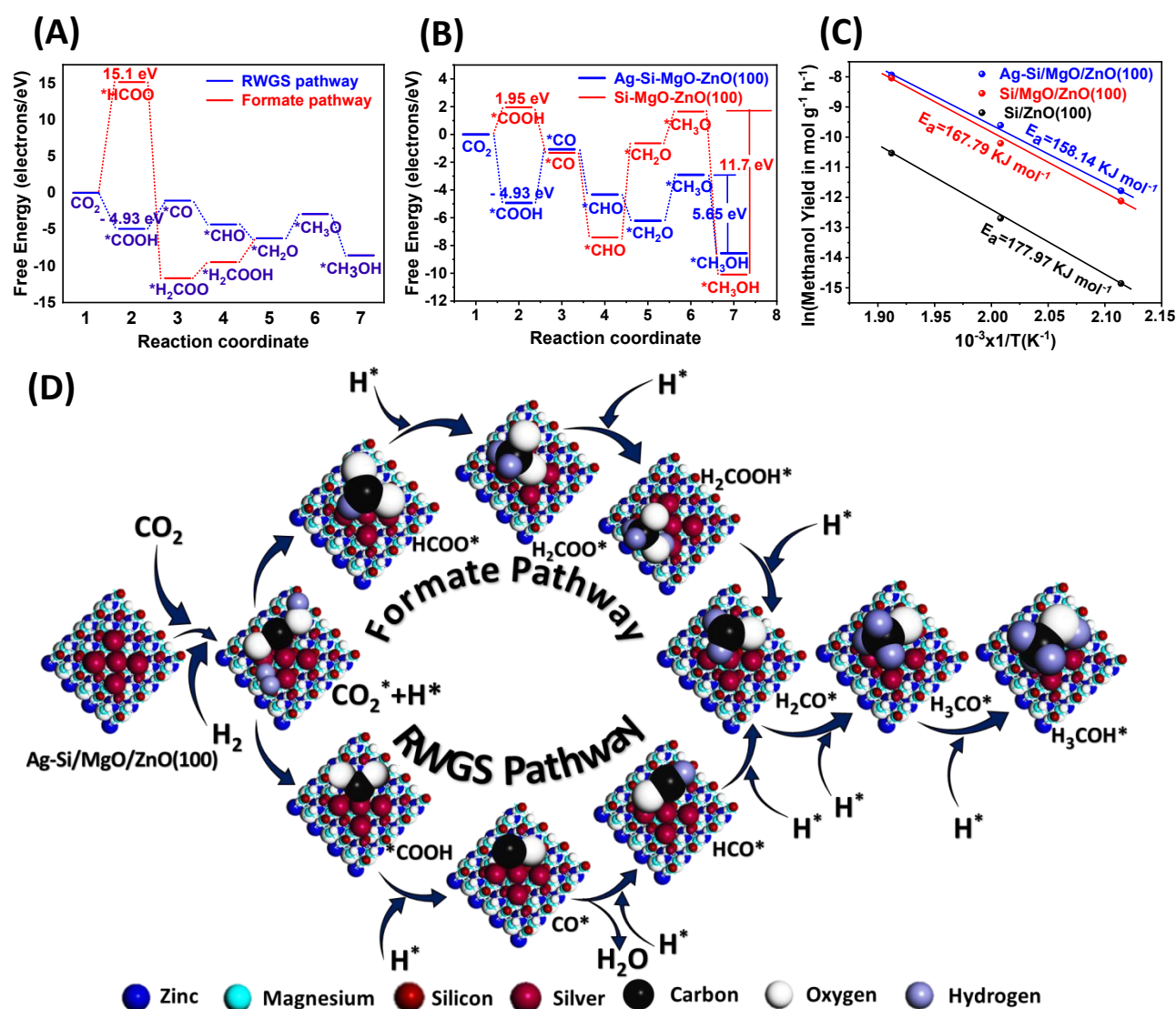
Fig. 3 XPS survey spectra of Ag-Si/MgO/ZnO; High-resolution XPS spectra of (A) Ag 3d, (B) Si 2p, (C) Mg 2p (D) Zn 2p (E) O 1s in Ag-Si/MgO/ZnO sample. DFT calculations of CO₂ reduction. F) The partial density of states for s and p-orbits of Ag-Si/MgO/ZnO, Si/MgO/ZnO, and Si/ZnO.

To understand the enhancement in photocatalytic performance after loading Ag and Si nanoparticles, finite-difference time-domain (FDTD) calculations were conducted in the visible range at different wavelengths (400 nm-800 nm) to simulate the local electric field distribution between the Ag and Si nanoparticle assemblies on MgO/ZnO with an interparticle distance of 2 nm (Fig. 4A and Fig. S4(A–F)). The electric field intensity distribution was visualized on a logarithmic scale. Fig. S4(G) shows the electric field distribution, |E|², around the surface of the Ag-Si/MgO/ZnO as a function of wavelength using FDTD simulations. Upon light irradiation, the electric field distribution |E|² around the surface of the Ag-Si/MgO/ZnO was enhanced, and a maximum value of |E_{max}|² of ≈ 800 was obtained at a wavelength of 457.143 nm. This improved local electric field, originating from the LSPR effect, was believed to have accelerated the transfer of hot electrons in the Ag–Si nanoparticles and promoted the separation of electron–hole pairs in MgO/ZnO. Furthermore, the visible-light absorbance was increased by Ag loading, thereby improving the photocatalytic activity, consistent with the photoluminescence results. The photocatalytic performance of the prepared samples was evaluated in a continuous-flow reactor system using CO₂ as the reactant at temperatures up to

300 °C and atmospheric pressure. The H₂/CO₂ ratio was maintained at 3:1. The results (Fig. 4B–F) showed that CH₃OH was the predominant product. At 160 °C, CH₃OH formation was detected under light irradiation, whereas no CH₃OH was observed under dark conditions. These results suggested that below 160 °C, the Ag–Si/MgO/ZnO nanocrystal superstructures could only catalyze the RWGS reaction. CH₃OH formation was most likely kinetically inhibited at low temperatures and pressures. The highest CH₃OH production rate was obtained at 250 °C, reaching 357.53 μmol g_{cat}⁻¹ h⁻¹ under light illumination (Fig. 4B and 4C). This value at 3 bar was higher than that produced over Si/MgO/ZnO and Si/ZnO composites by factors of 1.12 and 4.7, respectively. The as-prepared Ag–Si/MgO/ZnO photocatalyst exhibited a high apparent quantum yield (AQY) of 21.27% at an excitation wavelength of 420 nm for CH₃OH production, demonstrating its excellent visible-light-driven photocatalytic efficiency. When the temperature was increased to 300 °C, the CH₃OH production rate decreased to 121.84 μmol g_{cat}⁻¹ h⁻¹. This decline was attributed to the exothermic nature of CH₃OH synthesis (Eq. 1), which shifted the equilibrium toward the reactants at higher temperatures according to Le Chatelier's principle. The reaction thermodynamics at 300 °C favored the RWGS pathway, confirming that 250 °C was the optimal temperature for CH₃OH formation.



600 Fig. 4 A) FDTD simulation of the electric field distributions, $|E|^2$ around the surface of Ag-Si
 601 nanoparticles placed on MgO/ZnO excited by visible light at wavelength of 457.143 nm. Photo-
 602 thermo-catalytic performance: B) Temperature-dependent CH_3OH generation rate over
 603 Si/ZnO, Si/MgO/ZnO, and Ag-Si/MgO/ZnO photocatalysts under photo-thermal conditions.
 604 C) Influence of pressure on CH_3OH evolution rate over Ag-Si/MgO/ZnO under dark and light
 605 conditions; D) Influence of cooling temperature on methanol condensation in the reservoir; E)
 606 Stability performance of Ag-Si/MgO/ZnO photocatalyst in photocatalytic CO_2 hydrogenation
 607 to CH_3OH during continuous 72h at 250 °C and 3 bar pressure under irradiation of light; F)
 608 Methanol production rate as a function of GHSV over Ag-Si/MgO/ZnO; Reaction conditions:
 609 1 g of catalyst, 300 W lamp, 250 °C, and $\text{H}_2:\text{CO}_2 = 3:1$ for Fig. 5(C, E-F).



626 Fig. 5 DFT calculations of CO_2 reduction. (A) Free energy profiles of CO_2 to CH_3OH in
627 different pathways over Ag-Si/MgO/ZnO; (B) Free energy profiles of CO_2 to CH_3OH in COOH
628 pathway over Ag-Si/MgO/ZnO, and Si/MgO/ZnO; (C) Apparent activation energy (E_a)
629 evaluated using Arrhenius plots based on hydrogenation of CO_2 into methanol under light
630 condition; (D) Structural CO_2 hydrogenation pathways for methanol production within Ag-
631 Si/MgO/ZnO interface system.

632 A preliminary evaluation of the temperature-dependent solar CH_3OH production over
633 Ag-Si/MgO/ZnO is shown in Fig. 2b. The largest amount of CH_3OH was condensed between
634 $-8\text{ }^\circ\text{C}$ and $-16\text{ }^\circ\text{C}$ (Fig. 4D). The stability of the Ag-Si/MgO/ZnO photocatalyst was tested
635 during continuous operation for 72 h at $250\text{ }^\circ\text{C}$ and 3 bar under light irradiation (Fig. 4E). Only
636 a slight decrease in CH_3OH production rate was observed, indicating excellent long-term
637 stability. CH_3OH production rates of various photocatalysts and comparable systems are listed
638 in Table 2.⁵³⁻⁵⁹ A significant enhancement of CH_3OH generation from 159.84 to $357.53\text{ }\mu\text{mol}$
639 $\text{g}_{\text{cat}}^{-1}\text{ h}^{-1}$ achieved when the GHSV was increased from 120 to $480\text{ ml g}_{\text{cat}}^{-1}\text{ h}^{-1}$ at $250\text{ }^\circ\text{C}$ and 3
640 bar (Fig. 4F). This improvement was attributed to the synergistic effect of Ag-Si bimetallic
641 loading, consistent with previous findings by Chen et al.,⁴⁰ who reported that Ag doping
642 effectively suppressed electron-hole recombination and Si increased the catalyst surface area,
643 jointly promoting visible-light photocatalysis. Plasmonic enhancement had been imparted by
644 Ag because the optical response had been extended into the visible region and red-shifted
645 toward $\sim 630\text{ nm}$ after Ag incorporation, and stronger charge separation/transport had been
646 evidenced by pronounced PL quenching, higher transient photocurrent, and a smaller EIS
647 semicircle, indicating that a larger fraction of photoexcited electrons had been delivered to
648 surface reaction sites than in non-plasmonic semiconductor-only systems.⁶⁰ This behavior had
649 contrasted with common strategies such as band-gap narrowing by bulk doping or simple
650 heterojunction formation, where photon harvesting and interfacial electron flux had often
651 remained limited by weak visible absorption or fast recombination; in the present architecture,
652 plasmonic near-field/hot-carrier effects had been expected to raise the local excitation rate and
653 accelerate interfacial electron injection under visible irradiation, thereby increasing the
654 effective electron supply for CO_2/CO activation and hydrogenation.⁶¹

655
656
657

658 **Table 2:** Comparison of heterogeneous photocatalysts for hydrogenation of CO₂ into CH₃OH

Catalysts	T	P	V _{CO₂} :V _{H₂}	Methanol Yield	Reference
Au/In ₂ O ₃	-	-	3:1	320 μmol g _{cat} ⁻¹ h ⁻¹	53
CaCu ₃ Ti ₄ O ₁₂	250 °C	8 bar	3:1	308.5 μmol g _{cat} ⁻¹ h ⁻¹	54
Ru/In ₂ O ₃	-	atmP	3:1	280.4 μmol g _{cat} ⁻¹ h ⁻¹	55
Cu/ZnO	220 °C	atmP	2.5:1	127.8 μmol g ⁻¹ h ⁻¹	56
In ₂ O _{3-x} (OH) _y -NR-14h	250 °C	atmP	3:1	97.30 μmol g _{cat} ⁻¹ h ⁻¹	57
CoO/Co/TiO ₂	120 °C	atmP	3:1	39.6 μmol g _{cat} ⁻¹ h ⁻¹	58
H ₂ In ₂ O _{3-x} (OH) _y	300 °C	atmP	3:1	31.2 μmol g _{cat} ⁻¹ h ⁻¹	59
H ₂ In ₂ O _{3-x} (OH) _y	250 °C	atmP	3:1	14.92 μmol g _{cat} ⁻¹ h ⁻¹	59
Ag-Si/MgO/ZnO	250 °C	3 bar	3:1	357.53 μmol g _{cat} ⁻¹ h ⁻¹	This work

659

660 A schematic summary had been proposed in which CO₂ had been adsorbed at basic
 661 MgO. sites, COOH*/CO* formation had been favored at the Ag–Si/MgO/ZnO and terminal
 662 hydrogenation to CH₃OH had been completed predominantly at Ag sites supplied by efficiently
 663 separated photoelectrons under visible irradiation. The most favorable pathway for CO₂
 664 hydrogenation to CH₃OH over this interface system was determined. Formate (HCOO*) and
 665 carboxyl (*COOH) species were identified as the key intermediates in the HCOO* and RWGS
 666 pathways. The Ag–Si/MgO/ZnO(100) system demonstrated the most energetically favorable
 667 *COOH pathway, with the lowest barrier (−4.93 eV) and a strongly exothermic reaction energy
 668 for CH₃OH formation (−8.55961 eV). In contrast, the HCOO* pathway exhibited a high barrier
 669 (15.1 eV) and endothermic CO₂ → HCOO* conversion. Therefore, the *COOH route was
 670 identified as the preferred pathway over Ag–Si/MgO/ZnO(100) (Fig. 5A). Starting from
 671 *COOH, the Gibbs free-energy profiles for the 6H⁺/6e[−] reduction of CO₂ to CH₃OH over Ag–
 672 Si/MgO/ZnO(100) and Si/MgO/ZnO(100) were analyzed (Fig. 5B). CO₂ hydrogenation to
 673 *COOH was exothermic (−4.93 eV) over Ag–Si/MgO/ZnO(100) but endothermic (+1.95 eV)
 674 over Si/MgO/ZnO(100), demonstrating the greater favorability of COOH formation in the
 675 presence of Ag. Incorporation of MgO enhanced *COOH adsorption, enabling its conversion
 676 to *CO, which was readily hydrogenated to methoxy (CH₃O*), as also reported by Li et al.⁶²
 677 Compared with Si/MgO/ZnO, Ag–Si/MgO/ZnO had little effect on the free energies of
 678 *COOH→*CO, *CO→CHO, or *CHO→*CH₂O. However, the last three proton-transfer
 679 steps were identified as the decisive steps controlling performance. It was inferred that the first
 680 three intermediates were adsorbed on Si sites, while the final three were stabilized on Ag sites.

681 Partial density of states (PDOS) analysis at Ag sites demonstrated that Ag facilitated
 682 more rapid electron transfer from *CH₂O, accelerating its hydrogenation to *CH₃O. The free
 683 energy for the step CH₃O + H⁺ + e[−] → CH₃OH was reduced to 5.65 eV (Fig. 5B). Overall,
 684 CH₃OH formation over Ag–Si/MgO/ZnO proceeded predominantly via the pathway:

685 $^{*}\text{COOH} + \text{H}^{*} \rightarrow ^{*}\text{CO} + \text{H}^{*} \rightarrow ^{*}\text{HCO} + \text{H}^{*} \rightarrow ^{*}\text{H}_2\text{CO} + \text{H}^{*} \rightarrow ^{*}\text{CH}_3\text{O} + \text{H}^{*} \rightarrow \text{CH}_3\text{OH}^{*}$ View Article Online
DOI: 10.1039/D5SE01485A

686 which was both kinetically and thermodynamically preferred. This mechanism aligns with the
687 literature reported by Shan et al.,⁶³ where CO_2 was adsorbed and activated to CO_2^{*} ,
688 subsequently forming COOH^{*} and CO^{*} and undergoing stepwise hydrogenation to CH_3OH .
689 Both of the final steps were enhanced at the bimetallic sites, indicating that Ag–Si/MgO/ZnO
690 enabled more efficient and selective CO_2 conversion to CH_3OH . The apparent activation
691 energy for Ag–Si/MgO/ZnO was 158.14 kJ mol⁻¹, lower than that of Si/MgO/ZnO (167.79 kJ
692 mol⁻¹) and Si/ZnO (177.97 kJ mol⁻¹) under light irradiation (Fig. 5C). On the contrary, the
693 apparent activation energy for Ag–Si/MgO/ZnO under purely thermal conditions as a reference
694 was 172.48 KJ mol⁻¹, lower than that of Si/MgO/ZnO (184.51 kJ mol⁻¹) and Si/ZnO (201.38
695 kJ mol⁻¹) under dark condition (Fig. S5). The apparent activation energy that measured when
696 the system is not exposed to light (under dark conditions) is termed as the apparent activation
697 energy under purely thermal conditions. Because the reaction in this scenario entirely drives
698 by thermal energy, it is the appropriate baseline or reference condition to compare with the
699 photo-catalytic conditions (under light irradiation). A comparison of the apparent activation
700 energy (E_a) between light irradiation and dark condition reveals that light significantly reduces
701 the energy barrier for the reaction across all catalysts (Fig. 5C and Fig. S5). Under dark
702 conditions, the reaction relies solely on thermal energy to overcome the activation barrier. The
703 more significant values (172.48 KJ mol⁻¹) to (201.38 KJ mol⁻¹) (Fig. S5) appear the substantial
704 energy required to initiate the reaction without external photonic contribution. However, light
705 irradiation consistently lowers the activation energy through generating electron-hole pairs by
706 using photonic energy. These photo-induced charge-carriers efficiently reduce the thermal
707 threshold needed to achieve the transition state, facilitating redox processes at the surface. In
708 both circumstances, the synergistic impact of adding Ag and MgO further reduces this barrier.
709 The observed reduction of E_a for Si/MgO/ZnO compared to Si/ZnO under both light and dark
710 conditions was triggered by this modification that facilitated charge transfer easier and
711 provided more active sites. Although, Ag can maintain a lower E_a than its non-doped
712 counterparts in the dark by contributing in charge separation through defect levels. However,
713 Ag acts as an electron sink, trapping photo-induced electrons to prevent their recombination
714 with holes, which significantly boosted activity and lowered E_a under light condition. The
715 inclusion of Ag and Si bi-metals in the Ag–Si/MgO/ZnO catalyst creates a multifaceted
716 enhancement that reduced activation energy (E_a) more effectively than single-metal systems.
717 These results indicated that simultaneous Ag and Si doping significantly improved reactant



718 activation. The DFT calculations were therefore consistent with the experimental activity
719 trends.

720 Fig. 5D shows the structural CO_2 hydrogenation pathways for methanol production
721 within Ag–Si/MgO/ZnO interface system. Ag and Si had synergistically generated a dual-site
722 catalytic landscape on Ag–Si/MgO/ZnO(100), where the initial CO_2 activation had been
723 promoted through a COOH-mediated route that had been calculated as exothermic on Ag–
724 Si/MgO/ZnO(100) (−4.93 eV) but endothermic on Si/MgO/ZnO(100) (+1.95 eV). This
725 indicates that the bimetallic interface reduced the energy barrier for forming early oxygenated
726 intermediates compared with the Ag-free surface. The decisive hydrogenation sequence had
727 been described as spatially partitioned, such that early intermediates had been preferentially
728 stabilized at Si-associated interfacial/oxide sites while the late hydrogenation steps ($\text{CHO}^* \rightarrow$
729 CH_3OH) had been stabilized at Ag-rich sites acting as electron-accepting and hydrogenation
730 centers,

731 which had been consistent with the reported DOS features near the Fermi level.⁶⁴ This
732 mechanistic assignment had been directly linked to experimental observables because
733 suppressed recombination and improved charge transport had been evidenced by PL
734 quenching, increased transient photocurrent, and a smaller EIS semicircle for Ag–
735 Si/MgO/ZnO, and the same sample had delivered the highest methanol rate ($357.53 \mu\text{mol g}_{\text{cat}}^{-1}$
736 h^{-1} at 250°C and 3 bar) with the lowest apparent activation energy (158.14 kJ mol^{−1}), which
737 had been aligned with the computed facilitation of key elementary steps.⁶⁵

738 739 4. Conclusion

740 The Ag and Si–bimetal–doped MgO-promoted ZnO photocatalysts were synthesized via a
741 solid-phase reaction approach. Using the 10 wt.% Ag–Si/MgO/ZnO catalyst, the highest
742 CH_3OH production rate of $357.53 \mu\text{mol g}_{\text{cat}}^{-1} \text{h}^{-1}$ was achieved for CO_2 hydrogenation at 250°C
743 under light illumination. A strong interaction between ZnO and MgO, resulting in a
744 synergistic effect, could be responsible for the excellent selectivity of the 10 wt.% Ag–
745 Si/MgO/ZnO catalyst in the photocatalytic hydrogenation of CO_2 to CH_3OH . No significant
746 deactivation was observed after 72 h of reaction. CO_2 adsorption on the Ag–Si/MgO/ZnO(100)
747 surface (−1.04 eV) was 0.35 eV stronger than on Si/MgO/ZnO(100), which was inferred to
748 have enhanced CO_2 activation and promoted higher CO_2 conversion. The stronger adsorption
749 observed at the Ag–Si/MgO/ZnO(100) interface compared with the Si/MgO/ZnO(100)
750 interface was inferred to enhance CO_2 adsorption, thereby promoting higher CO_2 conversion



751 over the Ag–Si/MgO/ZnO(100) catalyst. This study thus provides new insights into the rational
752 design of photocatalysts with well-defined heterojunctions for efficient photocatalytic CO₂
753 reduction.

[View Article Online](#)
DOI: 10.1039/DSE01485A

754 **CRediT authorship contribution statement**

755 **AM:** Writing – original draft, Methodology, Formal analysis, Data curation; **A-TH:** review &
756 editing, Writing; **MTI:** Writing – review & editing, Validation; **MAH:** Writing – review &
757 editing; **TI:** Writing – review & editing, Writing – original draft, Visualization; **AI:** Writing –
758 review & editing, Writing – original draft, Supervision, Funding acquisition,
759 Conceptualization.

760

761 **Declaration of competing interest**

762 The authors declare that they have no known competing financial interests or personal
763 relationships that could have appeared to influence the work reported in this paper.

764 **Acknowledgments**

765 This work was supported by the Bangladesh Energy and Power Research Council
766 (BEPRC) under Research Grant No. March 27, 0000.000.39.001.17.651. The research was
767 conducted at the Hydrogen Energy and CO₂ Conversion Laboratory, Department of Petroleum
768 and Mining Engineering, Jashore University of Science and Technology, Jashore, 7408,
769 Bangladesh.

770

771 **References:**

- 772 1 P. Ndem, O. Biose, E. Effiong, S. Udegbe, J. E. Ukpebor, I. H. Ifijen and E. E. Ukpebor, Environ. Monit. Assess., 2025, 197(8), 925.
- 773 2 C. Zhang, J. Fang, Z. Han, P. Chen, X. Xu, K. Wang, Y. Shi and J. Liao, IScience, 2025, 28(8). 113127.
- 774 3 F. Yan, H. Chen, T. Chi, J. Lu, X. Shen, F. Xie, P. Wang and Z. Zhang, Chem. Eng. J., 2025, 520, 166450.
- 775 4 J. He, G. Tian, D. Liao, Z. Li, Y. Cui, F. Wei, C. Zeng and C. Zhang, J. Energy Chem., 2025.
- 776 5 J. Zhao, Z. Wen, R. Zhu, Z. Li, R. Ding, Y. Zhu, T. Gu, R. Yang and Z. Zhu, Chem. Eng. J. Adv., 2020, 3, 100029.
- 777 6 A. Baig, V. Goswami and Sonal, Asian J. Water Environ. Pollut., 2024, 21(6), 49–57.
- 778 7 F. A. Rafi, M. M. Rana, B. Agili and A. S. Al Shahrany, Eur. J. Eng. Res., 2025, 5(2), 1–15.
- 779 8 M. M. Rana, S. M. Alam, F. A. Rafi, S. B. Deb, B. Agili, M. He and M. H. Ali, IEEE Access, 2025.



787 9 M. M. Rana, F. A. Rafi, B. Agili and A. S. Al Shahrany, *Eur. J. Electr. Eng. Comput. Sci.* View Article Online
DOI: 10.1039/DSE01485A
788 2024, 8(2), 1–8.

789 10 S. Yasar Aurko, R. Salehdin, F. Allahma Rafi and K. Habibul Kabir, *Singapore: Springer*
790 *Nature Singapore*, 2023, 277–290.

791 11 Y. Yang, C. Shen, K. Sun, D. Mei and C. J. Liu, *ACS Catal.*, 2023, 13(9), 6154–6168.

792 12 Q. Wu, S. Liang, T. Zhang, B. Louis and Q. Wang, *Fuel*, 2022, 313, 122963.

793 13 C. Clavero, *Nat. Photonics*, 2014, 8(2), 95–103.

794 14 M. M. J. Li and S. C. E. Tsang, *Catal. Sci. Technol.*, 2018, 8(14), 3450–3464.

795 15 M.L. Brongersma, N.J. Halas and P. Nordlander, *Nat. Nanotechnol.*, 2015, 10(1), 25–34.

796 16 K.K. Ng and S.M. Sze, *Wiley-Interscience*, 2007.

797 17 H.A. Atwater and A. Polman, *Nat. Mater.*, 2010, 9(3), 205–213.

798 18 W. Sheng, J. Yang, X. Li, G. Liu, Z. Lin, J. Long, S. Xiao, L. Tan and Y. Chen, *Energy*
799 *Environ. Sci.*, 2021, 14(6), 3532–3541.

800 19 T. Kong, A. Liao, Y. Xu, X. Qiao, H. Zhang, L. Zhang and C. Zhang, *RSC Adv.*, 2024,
801 14(24), 17041–17050.

802 20 J. Zhao, B. Liu, L. Meng, S. He, R. Yuan, Y. Hou, Z. Ding, H. Lin, Z. Zhang, X. Wang and
803 J. Long, *Appl. Catal.*, B, 2019, 256, 117823.

804 21 A.O. Yusuf, R.Y. Tekle, H.K. Amusa and G. Palmisano, *Case Stud. Chem. Environ. Eng.*,
805 2025, 11, 101172.

806 22 M.T. Khalil, X. Wu, S. Liu, Y. Liu, S. Ashraf, R. Shen, H. Zhang, Z. Peng, J. Jiang and B.
807 Li, *Green Chem.*, 2025, 27(30), 9016–9054.

808 23 Z.J. Wang, H. Song, H. Pang, Y. Ning, T.D. Dao, Z. Wang, H. Chen, Y. Weng, Q. Fu, T.
809 Nagao and Y. Fang, *Appl. Catal.*, B, 2019, 250, 10–16.

810 24 J.L.G. Fierro, M.A. Peña and M.C. Alvarez-Galvan, *Supported Metal Catal.*, 2005, 229–
811 255.

812 25 V.D. Dasireddy and B. Likozar, *Renewable Energy*, 2019, 140, 452–460.

813 26 Q. Chen, S. Meng, R. Liu, X. Zhai, X. Wang, L. Wang, H. Guo and Y. Yi, *Appl. Catal.*, B,
814 2024, 342, 123422.

815 27 Q. He, Z. Li, D. Li, F. Ning, Q. Wang, W. Liu, W. Zhang, Y. Cui, J. Zhang and C. Liu,
816 *Mol. Catal.*, 2024, 558, 114008.

817 28 N. Joshi and S. Loganathan, *ACS Omega*, 2023, 8(14), 13410–13420.

818 29 R. Pothu, H. Mitta, P. Banerjee, R. Boddula, R.K. Srivastava, P.K. Kalambate, R. Naik,
819 A.B. Radwan and N. Al-Qahtani, *Mater. Sci. Energy Technol.*, 2023, 6, 484–492.

820 30 K. Sun, N. Rui, C. Shen and C.J. Liu, *J. Phys. Chem. C*, 2021, 125(20), 10926–10936.

821 31 H. Liu, M. Zhao, J. Guo, S. Sun, D. Li, D. He and Y. Lei, *ACS Sustainable Chem. Eng.*,
822 2025, 13(15), 5787–5795.

823 32 X. Zhang, H. Liu, Y. Wang, S. Yang, Q. Chen, Z. Zhao, Y. Yang, Q. Kuang and Z. Xie,
824 *Chem. Eng. J.*, 2022, 443, 136482.

825 33 Y. Wang, Y. Liu, L. Tan, X. Lin, Y. Fang, X.F. Lu, Y. Hou, G. Zhang and S. Wang, *J.*
826 *Mater. Chem. A*, 2023, 11(48), 26804–26811.

View Article Online
DOI: 10.1039/DSE01485A

827 34 Y. Wang, B. Su, S. Wang, L. Tan, G. Zhang, Y. Fang and X. Wang, *Angew. Chem. Int. Ed.*, 2025, e202508611.

828 35 A. Islam, S.H. Teo, M.R. Awual and Y.H. Taufiq-Yap, *J. Cleaner Prod.*, 2020, 244, 118805.

829 36 C. Hu, Z. Jiang, Q. Wu, S. Cao, Q. Li, C. Chen, L. Yuan, W. Yang, J. Yang and J. Peng, *Nat. Commun.*, 2023, 14(1), 4767.

830 37 H. Yu, F. Chen, X. Li, H. Huang, Q. Zhang, S. Su, K. Wang, E. Mao, B. Mei, G. Mul and T. Ma, *Nat. Commun.*, 2021, 12(1), 4594.

831 38 H.J. Freund and G. Pacchioni, *Chem. Soc. Rev.*, 2008, 37(10), 2224–2242.

832 39 S. Chen, B. Lv, D. Wu and Y. Xu, *J. Nanosci. Nanotechnol.*, 2013, 13(2), 1569–1573.

833 40 Q. Chen, W. Shi, Y. Xu, D. Wu and Y. Sun, *Mater. Chem. Phys.*, 2011, 125(3), 825–832.

834 41 I.H. Alsohaimi, A.M. Nassar, T.A.S. Elnasr and B. Amar Cheba, *J. Cleaner Prod.*, 2020, 248, 119274.

835 42 N.N. Vu, S. Kaliaguine and T.O. Do, *Adv. Funct. Mater.*, 2019, 29(31), 1901825.

836 43 N. Ojha, A. Bajpai and S. Kumar, *J. Colloid Interface Sci.*, 2021, 585, 764–777.

837 44 N. Ojha, A. Bajpai and S. Kumar, *Catal. Sci. Technol.*, 2019, 9(17), 4598–4613.

838 45 S. Tada, F. Watanabe, K. Kiyota, N. Shimoda, R. Hayashi, M. Takahashi, A. Nariyuki, A. Igarashi and S. Satokawa, *J. Catal.*, 2017, 351, 107–118.

839 46 R. Grabowski, J. Słoczyński, M. Sliwa, D. Mucha, R.P. Socha, M. Lachowska and J. Skrzypek, *ACS Catal.*, 2011, 1(4), 266–278.

840 47 I.C. Freitas, J.M.R. Gallo, J.M.C. Bueno and C.M. Marques, *Top. Catal.*, 2016, 59(2), 357–365.

841 48 G.F. Cerofolini, C. Galati and L. Renna, *Surf. Interface Anal.*, 2003, 35(12), 968–973.

842 49 S.H. Teo, A. Islam, Y.H. Taufiq-Yap and M.R. Awual, *J. Cleaner Prod.*, 2021, 313, 127909.

843 50 P. Devaraji, M. Mapa, H.M. Abdul Hakkeem, V. Sudhakar, K. Krishnamoorthy and C.S. Gopinath, *ACS Omega*, 2017, 2(10), 6768–6781.

844 51 N.M. Julkapli and S. Bagheri, *Rev. Inorg. Chem.*, 2016, 36(1), 1–41.

845 52 F. Meshkani and M. Rezaei, *Catal. Commun.*, 2011, 12(11), 1046–1050.

846 53 L. Wang, D. Yao, C. Zhang, Y. Chen, L. Amirav and Z. Zhong, *Chem Catal.*, 2024, 4(9).

847 54 Z. Jiang, Z. Yuan, P.N. Duchesne, W. Sun, X. Lyu, W. Miao, C.J.V. Pérez, Y. Xu, D. Yang, B. Huang and Y. Dai, *Chem Catal.*, 2023, 3(2).

848 55 B. Deng, H. Song, Q. Wang, J. Hong, S. Song, Y. Zhang, K. Peng, H. Zhang, T. Kako and J. Ye, *Appl. Catal., B*, 2023, 327, 122471.

849 56 Z.J. Wang, H. Song, H. Pang, Y. Ning, T.D. Dao, Z. Wang, H. Chen, Y. Weng, Q. Fu, T. Nagao and Y. Fang, *Appl. Catal., B*, 2019, 250, 10-16.

850 57 L. Wang, M. Ghoussoub, H. Wang, Y. Shao, W. Sun, A.A. Tountas, T.E. Wood, H. Li, J.Y.Y. Loh, Y. Dong and M. Xia, *Joule*, 2018, 2(7), 1369-1381.

851 58 Z.H. He, C.S. Jiang, K. Wang, Z.Y. Wang, N. Li, W.T. Wang and Z.T. Liu, *Catal. Today*, 2020, 356, 579-588.

865 59 Z. Zhang, C. Mao, D.M. Meira, P.N. Duchesne, A.A. Tountas, Z. Li, C. Qiu, S. Tang, *RSC Advances*, 2022, 13(1), 1512. [View Article Online](#)
DOI: 10.1039/DSE01485A

866 Song, X. Ding and J. Sun, *Nat. Commun.*, 2022, 13(1), 1512.

867 60 S. Linic, P. Christopher and D.B. Ingram, *Nat. Mater.*, 2011, 10(12), 911-921.

868 61 M.L. Brongersma, N.J. Halas and P. Nordlander, *Nat. Nanotechnol.*, 2015, 10(1), 25-34.

869 62 K. Li and J.G. Chen, *ACS Catal.*, 2019, 9(9), 7840-7861.

870 63 X. Shan, G. Zhang, Y. Zhang, S. Zhang, F. Guo and Q. Xu, *Catalysts*, 2024, 14(11), 756.

871 64 J. Greeley, T.F. Jaramillo, J. Bonde, I.B. Chorkendorff and J.K. Nørskov, *Nat. Mater.*, 2006, 5(11), 909-913.

872 65 Z. Zeng, K.C. Chang, J. Kubal, N.M. Markovic and J. Greeley, *Nat. Energy*, 2017, 2(6), 17070.

873

874

Data availability statement

The data that support the findings of this study are available from the corresponding authors upon reasonable request.